Efficient non-noble Ni–Cu based catalysts for the valorization of palmitic acid through a decarboxylation reaction

Camila P Ferraz, Anouchka Kiméné, Karen Silva Vargas, Svetlana Heyte, Claire Durlin, Olivier Simon, Franck Dumeignil, Sébastien Paul, Robert Wojcieszak

Efficient non-noble Ni-Cu based catalysts for the valorization of palmitic acid through decarboxylation reaction

Camila P. Ferraz[a], Anouchka Kimene[a], Karen Silva[a], Svetlana Heyte[a], Claire Durlin[b], Olivier Simon[b], Franck Dumeignil[a], Sébastien Paul[a], Robert Wojcieszak[a]*

[a] Univ. Lille, CNRS, Centrale Lille, Univ. Artois, UMR 8181 - UCCS - Unité de Catalyse et Chimie du Solide, F-59000 Lille, France.

[b] Weylchem Lamotte S.A.S, Rue du Flottage, B.P. 1, 60350 Trosly Breuil, France

*corresponding author: robert.wojcieszak@univ-lille.fr

Abstract

Deoxygenation reactions, especially decarboxylation (DCX), are generally carried out with noble metal catalysts (Pt and Pd). Development of non-noble metal catalysts is highly desirable. For this purpose, non-noble monometallic catalysts (Ni, Fe, Cu, and Ag) and Ni-based bimetallic catalysts were studied for the DCX of palmitic acid (PA). Ni-Cu/C systems were by far the most advantageous, the presence of Cu prevents deactivation of the catalyst, decreases the reduction temperature, and significantly improves the yield of n-pentadecane. The higher Ni content in the 10%Ni10%Cu/C catalyst resulted in a higher proportion of

metallic Ni on the surface and higher charge transfer from Ni to Cu. Thus, the best catalytic performance with full PA conversion and 95% selectivity to n-pentadecane (PD) in 6 h was obtained at 320 °C, using 10 vol% of H_2 in N_2 and an operating pressure of 40 bar. Furthermore, this catalyst exhibited excellent recyclability under similar reaction conditions.

KEYWORDS. Decarboxylation; palmitic acid; n-paraffines; pentadecane; Ni-Cu catalyst;

1. Introduction

The continuously increasing world energy demand (+2.9% in 2018, the fastest since 2010) has driven the high utilization of fossil resources that today represent 85% of the global primary energy consumption (coal, oil, and natural gas) [1-3]. Besides being insufficient to satisfy the energy needs of a developing society, the imminent depletion of fossil resources and the anthropogenic climate change because of greenhouse gas emissions are of major concerns [4-6].

Thus, the exploitation of renewable resources represents an alternative towards a sustainable development and an answer to this growing energy demand. Due to their global abundance they are considered as a suitable feedstock for a variety of applications in different fields of human activities, such as fuels (biofuels), energy (biomass heat and biogas), and chemicals (polymers, fertilizers, pesticides, solvents, lubricants, pharmaceuticals, detergents, hygiene products, and cosmetics, etc. [7-8]). Vegetable oils, which are mainly composed of a mixture of triglycerides, are currently the subject of intense research worldwide. This is because they can produce straight chain alkanes ranging from C_8 to C_{18} (*n*-paraffins) that can be used for the production of biodiesel [9-10], green diesel [11-14], or aviation fuel [15-16]. Heavy Normal Paraffin (HNP), which refers to long-chain *n*-paraffins (C_{12} to C_{18}), are suitable for the pharmaceutical, cosmetics and food industry to manufacture relatively high viscosity products like ointments, creams, laxatives, protective coatings, and machinery lubricants [17-18]. Moreover, the production of biosourced HNP is also of high interest for the manufacture of biosourced and biodegradable detergents [19-20], which are nowadays mainly produced from petroleum [21].

Consequently, commercial processes for triglyceride hydroconversion into *n*-paraffins were developed [16]. It requires multistage processing by 1) hydrogenating the unsaturated moieties, 2) cracking to form fatty acids (FAs), where the hydrogenated triglycerides are hydroconverted into FAs and propylene, and 3) hydrogenating the fatty acids [16]. The last step requires the deoxygenation (DO) of the FAs through decarboxylation (DCX), decarbonylation (DCN), or hydrodeoxygenation (HDO) [22-23]. The catalytic DO of FAs has been extensively studied for many years [22, 24-28] and is yet the subject of research aiming at more economically viable processes for the production of biosourced hydrocarbons and biofuels. Besides being the main approach to produce *n*-paraffins, HDO requires the use of refined oil as substrate and high amounts of hydrogen, which increases the biofuel production costs [29-30]. Additionally, to improve catalytic HDO performances often requires the use of expensive noble metal catalysts (generally Pd and Pt) [5, 31-33].

DCX of FA using carbon-supported metallic catalysts has attracted much attention, wherein noble metal-based catalysts play an important role. Their use under high-pressure of hydrogen or carbon dioxide enhanced the feedstock conversion and liquid products yield [6, 10, 15, 39-41]. Among all catalysts studied, Pd and Pt-based catalysts showed best catalytic performances to hydrocarbons. Unfortunately, unfavorable price/abundance ratio and the rapid deactivation of these catalysts [42] are major drawbacks for industrial application. Therefore, finding a less expensive catalyst showing similar catalytic performances is a challenge. Non-noble based-catalysts such as Cu [29, 43], Ni[10, 15, 29, 36, 44] and Co [29] have been developed for DO of fatty acids, being the Ni-based supported catalysts the most efficient. DCX of SA using Ni/C was studied for some research groups [29, 36] that report up to 80% conversion and 81% of selectivity to (*n*-C_{17}) at 300 °C under H_2 when using 20%Ni/C. However, quantitative conversion and 97% of selectivity to C_{17} was achieved when using lower Pd loading (5%Pd/C) and concentration of hydrogen (10%H_2/N_2). Better result

was reported by Wu *et al.* [29] that studied DCX of SA wherein full conversion and 80% of selectivity to C_{17} was obtained under inert gas. Although the inert atmosphere represents a decrease in the cost of the process, this result was obtained at 370 °C, 70 °C above the temperature used with Pd/C (300 °C) [29]. Furthermore, the selectivity obtained with the Pd-catalyst is also higher (99% vs 80% with Ni/C) even if it presents lower metal loading (5%Pd/C vs 20%Ni/C) [45]. Ni/C showed very promising results; nevertheless, an improvement in catalytic performance is still desired for this reaction. Several papers report the enhanced of properties when combining two metals in a bimetallic system. In general, it leads to an electronic promotion, which could be beneficial for the catalytic activity. The alloying of Ni with Cu have shown promising results in different domains, although other non-noble metals have been used as second metal in Ni catalysts [46]. To the best of our knowledge, there are no reports of non-noble bimetallic catalysts for the DCX of FA.

Therefore, the present paper focuses on the development of non-noble metal catalysts presenting high activity, selectivity, and stability for the DCX of palmitic acid (PA), a saturated long-chain fatty acid originating from oleaginous biomass, to produce *n*-pentadecane. A series of mono- and bimetallic Ni-based supported catalysts have been prepared[47]. The active Ni-Cu/activated carbon (AC) catalysts were characterized and tested at different reactions conditions to obtain optimized conditions, insights into the reaction mechanism and to verify the recyclability of the catalyst.

2. Experimental

2.1. Catalysts preparation

The metal precursors (nickel nitrate hexahydrate (Ni(NO3)2·6 H2O, 97%); copper nitrate trihydrate (Cu(NO3)2·3 H2O, 99–104%); iron nitrate nonahydrate (Fe(NO3)3·9

H2O, ≥99.999% trace metals basis) and silver nitrate (Ag(NO3), ACS reagent ≥99.0%)), the substrates tested ((PA, >99% and SA for synthesis, ≥ 97.0%), hexadecane (ReagentPlus®, 99%), the gas chromatography (GC) standards (hexane (analytical standard, ≥99.7%) and pentadecane, ≥98.0% (GC)), the internal standard (toluene (GC-MS SupraSolv®, ≥ 99.8 %)), activated carbon as support (Darco KB-g pore volume = 1.1 cm^3/g and specific surface area = 1290 m^2/g), and hydrazine as reductant (78–82% in aqueous solution) were all purchased from Sigma-Aldrich and used as received.

A series of monometallic and bimetallic catalysts supported on activated carbon were synthesized by the chemical reduction with hydrazine (Ni/C, Ag/C, Cu/C, Fe/C Ni-Ag/C, Ni-Cu/C, and Ni-Fe/C) using the Chemspeed CatImpreg HT robot (REALCAT platform) using method described in [47]. The conditions of the synthesis are summarized in Table 1. The monometallic catalysts are noted as 10%Me (where Me = Ni, Ag, Cu, and Fe), indicating the theoretical weight mass (%) of the loaded metal on the catalyst. Bimetallic catalysts were denoted similarly as 10%Ni10%Me where Me = Ag, Cu and Fe, and Ni-based catalysts as x%Nix%Cu where x = 5, 10, and 15% in weight mass of Ni and Cu.

Table 1. Salt precursor solutions used for the synthesis and the final pH of the solution.

catalyst	*V Ni solution (mL)*	*V Ag solution (mL)*	*V Cu solution (mL)*	*V Fe solution (mL)*	*Final pH*
10%Ni/C	1.04	-	-	-	10
10%Ag/C	-	0.7	-	-	9.3
10%Cu/C	-	-	1.06	-	9.4
10%Fe/C	-	-	-	1	9.6
10%Ni10%Ag/C	1.17	0.79	-	-	10
5%Ni5%Cu/C	0.52	-	0.53	-	9.6
10%Ni10%Cu/C	1.17	-	1.19	-	9.6
15%Ni15%Cu/C	2.01	-	2.04	-	9.4
10%Ni10%Fe/C	1.17	-	-	1.13	10.6

2.2 Catalyst characterization

The surface area, pore volume and distribution of the pore size were determined by nitrogen adsorption/desorption at -195,65 °C using a TriStar II Plus and a 3Flex apparatus from

Micromeritics. Preliminary degassing of the samples was performed at 150 °C for 45 min. The specific surface area (BET) was evaluated using the BET method (Brunauer, Emmet and Teller). In addition, the pore size distribution and the pore volume were calculated according to the Barrett-Joyner-Halenda (BJH) formula taking into account the desorption branch.

TEM electron microscopy images were recorded on electron microscope FEI Tecnai G2 20 (TEM) equipped with an EDX (Energy-dispersive X-ray spectroscopy) micro-analysis, a Gatan energy filter (EELS), precession and electron tomography systems and an Orius CCD camera. The average Au nanoparticle size was determined taking into account at least 300 particles.

XPS spectra were collected on a high-performance hemispheric analyzer on a XPS Kratos, Axis UltraDLD "2009" with monochromatic Al Kα ($h\nu$ = 1486.6 eV) radiation as the excitation source. For interpretation the calibration of the XPS spectra was made using the carbon C 1s reference of 284.8 eV.

X-ray fluorescence spectroscopy (XRF) was recorded on a M4 Tornado from Bruker. To obtain accurate quantification of the metals present in the catalysts, each sample was irradiated 30 times in order to cover the whole catalyst surface. The mean value of the metal content was then determined.

The X-ray powder diffractograms were recorded on a D8 Discover X-Ray Diffractometer from Bruker using a X-Ray tube in Cu (Kα) radiation (λ=1.54060 Å) in the 10-70° range with steps of 0.02° per second. Diffrac Eva software was used for the identification of the crystalline phases. The average crystallite size of the metals particles in the catalyst was determined by the Scherrer equation.

The ICP-OES (Inductively Coupled Plasma Optical Emission Spectrometry) analysis was performed using Agilent 720-ES ICP-OES equipment combined with Vulcan 42S automated digestion system.

The TPR (Temperature programmed reduction with H_2) analyses were performed on an automated AutoChem II 2920 Chemisorption Analyzer from Micromeritics. 40 mg of catalyst were flushed with a mixture gas of 5 vol.% H_2 in Ar at room temperature. Temperature of the sample was increased linearly up to 750 °C.

2.3 Catalytic tests

Catalytic tests were carried out in a screening pressure reactor (SPR) from Freeslate, which is a system equipped with 24 parallel stainless-steel batch reactors of 6-mL volume each. All catalysts (12.8, 26, 52, or 75 mg) were activated prior to the catalytic tests in the SPR device. Activation was performed *in situ* under pure H_2 (30 mL/min) at 2 bar for 3 h. The temperature ramp was 5 °C/min up to 350 °C. After activation, the reactor vessel containing the hermetically sealed batch-reactors was transferred to a glove box. The reactors were then loaded with the solvent (hexadecane, 1.5 g) and the substrate (0.197 mmol of palmitic acid (50.5 mg) or stearic acid (56.0 mg)). Then, the reactors were hermetically resealed and reconnected to the SPR unit for the catalytic tests. The catalytic DCX of PA was carried out at 250, 300 or 320 °C using an initial pressure of 20 bar (40 bar under operating conditions) using 10 vol% of H_2 in N_2 or under pure N_2. The pressure and the temperature throughout the reaction were kept constant for 1.5, 3, 6, or 12 hours applying orbital stirring (600 rpm). At the end of the reaction, the reaction mixtures were collected and heated to 80 °C under ultrasound in order to avoid the crystallization of unconverted PA, filtered to remove the catalyst and diluted for GC-analysis. Then, 20 µL of the reaction mixture and 100 µL of toluene (internal standard) were added to a vial and diluted with hexane to a final volume of 1 mL. Before the samples were injected on the GC, the vials were heated to 40 °C in order to keep the homogeneity of the solution. A Shimadzu GC-2010 Plus gas chromatograph

equipped with a flame ionization detector (FID) and a ZB 5MS column (30 m × 0.25 mm × 0.25 μm) was used for the analysis of the products.

3. Results and discussion

3.1. Non-noble monometallic and Ni-based bimetallic catalysts

To achieve our goal to identify active non-noble catalysts for the DCX of PA into *n*-PD, four different carbon-based non-noble metal catalysts were studied first. Among them, nickel and iron were considered, which are 4,000 and 10,000 times less expensive than platinum, respectively. Similarly, copper and silver, which are 3,000 [48] and 140 [49] times less expensive than palladium but more abundant, were also tested. The activated carbon-supported catalysts loaded with 10 wt% metal were tested at the same reaction conditions. Figure 1a displays the PA conversion, *n*-PD selectivity, yield, and the carbon balance obtained in these preliminary tests. Considered as promising catalyst for the DCX reaction, the Ni-based catalyst 10%Ni/C was the most active with 57% conversion. However, it was also the least selective catalyst, with only 20% selectivity to *n*-PD. This is because Ni is a versatile metal. Ni-catalysts are active for several reactions such as dehydrogenation and C–C bond cleavage [46]. Despite that, no more than a 11% *n*-PD yield was observed using any of these non-noble metal catalysts, even if the 10%Cu/C catalyst presented the highest selectivity (44%), followed by 10%Ag/C (31%) and 10%Fe/C (26%). The alloying of metals is a known strategy to overcome issues related to catalytic performances. Bimetallic catalysts are recognized for combining the different metals at the atomic level such that the proprieties can be tuned. Thus, the addition of a second metal to form bimetallic catalysts could result in a significant improvement in the catalytic activity of Ni-based catalysts besides the increase in stability [50-54]. Thus, a series of Ni-based bimetallic catalysts was synthesized and tested for

the DCX of PA to *n*-PD. The results presented in Figure 1b shows the catalytic performances of the Ni-based catalysts with respect to the second metal. According to the results, the combination of the other metals with Ni was beneficial with the exception of Fe, where the 10%Ni10%Fe/C catalyst performed similar to the monometallic 10%Fe/C catalyst. The Ni-Ag combination improved the catalytic activity, but when Ni was combined with Cu (10%Ni10%Cu/C) the best catalytic performance was obtained with respect to the three bimetallic catalysts tested. The bimetallic Ni-Cu was the most efficient, providing high conversion (76%) and selectivity (87%). Therefore, the Ni-Cu bimetallic catalysts were studied in more depth. In order to obtain the best catalytic performance when using Ni-Cu catalysts, other Ni-Cu compositions were prepared, varying the Ni and Cu contents. The total theoretical loading of Ni and Cu on the activated carbon ranged from 10–30 wt%, *i.e.* 5%Ni5%Cu, 10%Ni10%Cu and 15%Ni15%Cu aiming at a constant Ni:Cu weight ratio of 1. The three Ni-Cu bimetallic catalysts were prepared and tested, however the metal loading is referred to as the theoretical metal loading (5%Ni5%Cu/C, 10%Ni10%Cu/C and 15%Ni15%Cu/C). The actual metal loading was analyzed and is discussed at a later stage. The catalytic results depicted in Figure 1 c show the effect of Cu loading on the DCX activity for PA. Considering a total metal loading of 10% (10%Cu, 10%Ni and 5%Ni5%Cu/C catalysts), the bimetallic catalyst presented a higher selectivity (31%), but a lower conversion (39%) than the monometallic 10%Ni and 10%Cu catalysts. This already highlights the bimetallic effect. However, when the total metal content increased, as in the case of the 10%Ni10%Cu/C catalyst, the effect of the Ni-Cu promotion was even more evident. The enhancement in PA conversion and *n*-PD selectivity (76% and 87%, respectively) resulted in *n*-PD yields up to 66%. In addition, the carbon balance was almost 90%, indicating that the number of unknown byproducts formed was small. However, increasing the Cu content to 15% with respect to a total metal loading of 30% (15%Ni15%Cu/C), the catalytic efficiency

decreased providing only a 65% PA conversion and 42% *n*-PD selectivity. Considering the best catalytic performance exhibited by the 10%Ni10%Cu/C catalyst, characterization studies were conducted to understand and determine the active phases.

The results exhibited in **Table 2** correlate the theoretical and experimental values for the metal content in the monometallic and bimetallic catalysts supported on activated carbon. Using ICP-OES analysis, 10%Cu/C presented exactly the Cu content added, whereas for 10%Ni/C a slightly lower metal content was obtained. For the 5%Ni5%Cu/C catalyst, the experimental Ni and Cu content (0.46:0.54 wt or 0.48:0.52 mol) was very similar to the theoretical values (0.5:0.5 wt or 0.52:0.48 mol). By increasing the metal content, however, different metal loadings were observed. For 10%Ni10%Cu/C, the Ni content was close to 10%, while the Cu content was much lower (6.5%) affording a Ni-rich catalyst (0.63:0.37 wt or 0.65:0.35 mol). A Ni:Cu ratio of 1.5 was also observed by EDX, proving that a higher Ni amount was obtained for this catalyst. On the contrary, for higher metal content catalysts (15%Ni15%Cu/C), the Cu content was closer to the expected value (14.5%) and the Ni content was nearly half of the theoretical value (8.5%). Thus, a Cu-rich bimetallic catalyst was obtained (0.37:0.63 wt% or 0.39:0.61 mol%). The differences observed in the Ni and Cu content of the bimetallic catalysts was related to the properties of the support that adsorbed the metals in an unequal manner presenting a metal loading limitation depending on the metal concentration. This affected the thermodynamics involved in the formation of the bimetallic solutions, because various structural arrangements are possible with respect to the combination of the two metals, varying from a solid homogenous Ni-Cu solution to metal particles with segregated phases [55-56]. Thus, even if the same synthetic procedure and reaction conditions were applied to synthesize all catalysts, different Ni:Cu compositions were observed, which resulted in different structural arrangements for the bimetallic catalysts.

The textural properties presented in **Table 2** are affected by the deposition of Ni and Cu at different loadings. The specific surface area observed for the catalysts were lower compared to that of the pure activated carbon. Once the metal particles were deposited on the support they decreased the specific surface area. However, only a slight decrease in the mean pore volume was observed for the bimetallic catalysts in comparison with the pure activated carbon. Thus, it was assumed that the metal particles hardly filled the pores. Comparing the monometallic catalysts, 10%Cu/C presented the highest surface area, which indicated a higher mean particle size. The BET of the bimetallic catalysts decreased compared to the pure constituents and the monometallic versions, confirming the positive effect of the Ni-Cu mixture on particle size control. Among the Ni-Cu catalysts, a decrease in the surface area was observed increasing the Ni content in the catalysts, as observed for 10%Ni10%Cu/C catalyst. This catalyst exhibited the lowest specific surface area and the highest Ni content (10.9% by ICP), corresponding to the smallest particle size. This suggested that the mean particle size was mainly affected by the Ni content of the bimetallic catalyst, as the increase in Cu content did not follow the trend of decreasing surface area. Owing to its improved textural features, the 10%Ni10%Cu/C catalyst was selected for further investigation.

Table 2. Textural properties and chemical composition of the support and Ni-Cu catalysts.

Catalysts	Theoretical metal loading (wt%)		Metal loading by ICP (wt%)				BET (m^2/g)	Mean pore size (Å)	Total pore volume (cm^3/g)
	Ni	Cu	Ni	Cu	Ni:Cu ratio (wt)/ Ni:Cu	Ni:Cu ratio (mol)			
Pure carbon							1290	67	0.68
10%Cu	-	10	-	10.3 ±0.4	-	-	1073	67	0.60
10%Ni	10	-	7.6 ± 0.2	-	-	-	877	67	0.51
5%Ni5%Cu	5	5	5.2±0.2	6±0.2	0.46:0.54/0.9	0.48:0.52	830	64	0.47
10%Ni10%Cu	10	10	10.9±2.2	6.5±1.5	0.63:0.37/1.7 (1.5)[a]	0.65:0.35	536	66	0.39
15%Ni15%Cu	15	15	8.5±0.3	14.5±0.7	0.37:0.63/0.6	0.39:0.61	645	64	0.39

[a]: Ni:Cu ratio (wt) obtained by EDX.

TEM analysis of the 10%Ni10%Cu/C catalyst (Figure 2) was performed and confirmed the presence of small spherical shaped metal particles ranging from approximately 2 to 6 nm, homogeneously distributed over the support with a mean value of 3.0 ± 0.6 nm (Fig. 2 a). Figure 2b shows the typical image of the activated 10%Ni10%Cu/C catalyst (at 350 °C under hydrogen for 2 h). Usually, the activation under H_2 before the catalytic reaction (activated catalyst) leads, in most of the cases, to particle growth and/or agglomeration [57]. In this case, no particle agglomeration was observed besides the growth of the particles to 20–25 nm with an average particle size of 17.1 ± 3.7 nm.

XRD analysis was performed on mono- and bimetallic catalysts in order to determine the different crystalline structures of the metals dispersed on the support. Figure 3a displays the XRD diffractograms of the fresh catalysts. In the monometallic 10%Cu/C catalyst the Cu species were already reduced without any indication of copper oxide, with two large diffraction peaks at 43.5° and 50.6°, corresponding to the (111) and (200) diffraction planes of the reflection of Cu^0 with a lattice parameter of 3.6122 Å (PDF 00-003-1005). In contrast, the XRD pattern of the as-prepared 10%Ni/C showed several peaks of weak intensity indicating the presence of complex forms of nickel species, but not NiO that presents three distinct diffraction peaks at 2θ = 37°, 44.3°, and 62.9°. The XRD patterns of the fresh Ni-catalyst displayed several peaks (41.4°, 45.4° and 46.3°), suggesting the presence of Ni-hydrazine structures (PDF-00-054-1419) formed during the catalyst synthesis, meaning that the Ni was not fully reduced by hydrazine, unlike Cu. The formation of Ni-complexes is known and their decomposition into metal powder in contact with air in the temperature range of 70 to 200 °C was reported (PDF 00-054-1419) [43]. For the bimetallic catalysts, the diffraction peaks assigned to Ni-hydrazine decreased with the increase in Cu-content (10%Ni10%Cu/C with Ni:Cu = 0.65:0.35 mol) and disappeared for 5%Ni5%Cu/C and 15%Ni15%Cu/C catalysts presenting higher amounts of Cu (Ni:Cu = 0.48:0.52 and 0.39:0.61

mol, respectively (Figure 3a). The catalysts provided two diffraction peaks for the (111) and (200) planes, positioned between those of Ni-hydrazine and metallic Cu, indicating the formation of a bimetallic $Ni_{0.04}Cu_{0.96}$ structure stabilized with N-species (PDF-04-003-7052). This is because hydrazine used in the catalyst synthesis may act as a reducing agent and its decomposition products also act as a capping ligand. The position of the diffraction peaks was related to the Ni:Cu ratio, which gradually shifted towards a higher 2θ value with the increase in Cu content. For 15%Ni15%Cu/C, with the highest Cu content (Ni:Cu = 0.39:0.61 mol), the diffraction peaks shifted closer to Cu^0, whereas for 5%Ni5%Cu/C and 10%Ni10%Cu/C the peaks were observed at a lower angle. Thus, in the fresh catalysts, a high Cu content favors the formation of Ni-Cu alloys while in high Ni content catalysts Ni-Cu alloy and Ni-hydrazine species were observed. The XRD patterns and the XRD peak of the (111) plane in Ni-Cu bimetallic catalysts after activation with hydrogen are depicted in Figure 3b and c. For the 10% Cu/C catalyst, the activation treatment only slightly shifted the peaks assigned to Cu^0 observed at 43.47° and 50.38° (PDF 00-002-1225), but for 10% Ni/C, Ni-hydrazine species were reduced and only metallic Ni was observed at 44.36° and 51.69° (PDF 00-001-1258). For the bimetallic catalysts after activation under hydrogen, a shoulder at higher angle was observed in all cases, indicating a second peak. This might be related to the segregation of Ni in the Ni-Cu alloy, which, according to literature, is promoted upon annealing in H_2 [58]. By comparing the XRD patterns of metallic Ni and Cu with those of bimetallic catalysts a clear shift is observed, indicating the formation of different Ni-Cu alloys instead of individual Ni and Cu NPs. Figure 3c shows that the catalysts contain two bimetallic phases with different compositions corresponding to Cu-rich and Ni-rich phases. The higher the Ni content, the higher the relative intensity of the Ni-rich phase, the most intense one was observed for 10%Ni10%Cu/C. Moreover, the positive shift of the Ni-rich phase in the Ni-Cu alloy peaks from 43.7° for 5%Ni5%Cu/C to 44.3° for 10%Ni10%Cu/C indicated a higher Ni proportion

in the shell region of the surface, according to Vegard's law [59-60]. Similar results were reported by other research groups [61-63] that observed different segregation characteristics for a specific Ni:Cu composition by changing the synthetic method. In our case, the same effect was obtained by changing the metal loadings. Therefore, it is reasonable to assume that the high Ni-content favored different Ni-rich and Cu-rich phases, while in catalysts of higher Cu-content the Ni-Cu alloy characteristics predominated.

The identification of the metal species on the surface and their compositions are important to understand the relation between structure and activity with regards to the DCX of PA. Therefore, the surface composition of three activated bimetallic Ni-Cu catalysts (5%Ni5%Cu/C; 10%Ni10%Cu/C; 15%Ni15%Cu/C) and one monometallic catalyst (10%Cu/C) were analyzed by XPS. Figure 3d–f depicts the XPS spectra in the Cu 2p and Ni 2p region for the bimetallic Ni-Cu catalysts after activation with hydrogen at 350 °C for 2 h (d and e), and the spectra in the Ni $2p_{3/2}$ region for 10%Ni10%Cu/C catalyst (f). The binding energies (BEs) of the Cu $2p_{3/2}$ and Ni $2p_{3/2}$ regions of the mono- and bimetallic catalysts are summarized in **Table 3**. For all samples, mono- and bimetallic catalysts, the Cu 2p spectra revealed two clearly defined peaks at 932.5–932.8 ($2p_{3/2}$) and 952.3–952.5 eV ($2p_{1/2}$), which were attributed to metallic copper, due to the absence of shake-up satellite peaks (Figure 3d).[50,59,64] In addition, the analysis of the CuLMM Auger kinetic energy (one peak at 918.5 eV) indicated the presence of metallic copper on the catalysts surface (**Table 3**). Thus, for both the 10%Cu/C and the Ni-Cu bimetallic catalysts, the Cu-species on the surface are in metallic state after activation with hydrogen, although lower BEs were observed for the bimetallic catalysts compared to 10%Cu/C. The BE for Cu peaks showed that the higher the Cu content, the lower the binding energy. The Ni 2p XPS spectra displayed two peaks centered at 852.6–852.8 ($2p_{3/2}$) and 869.9–870.2 eV ($2p_{1/2}$), indicating that the bimetallic catalysts are dominated by metallic state Ni, even though the presence of shake-up satellites

(sat.) suggested that part of the surface or near-surface Ni atoms were oxidized (Figure 3e) [50, 59, 64]. The deconvolution of the peak in the Ni $2p_{3/2}$ region were attributed to two components for all the samples with BEs in the range of 852.6–852.8 eV and 853.3–854.0 eV (Figure 3f). The component at the lower BE corresponded to Ni^0 and the component at higher binding energy to Ni^{2+} or possibly the Ni^0 in the Cu-rich phase of the Ni-Cu alloy. The BE of Ni^{2+} in NiO or $Ni(OH)_2$ is usually reported as > 855.0 eV [50, 65-66]. In **Table 3**, the proportion of metallic Ni at the surface of all Ni-species (Ni^0/(Ni^0 +Ni-species) is presented. Accordingly, for all Ni-Cu catalysts, most of the Ni is in metallic form (Ni^0/(Ni^0 +Ni-species > 50%), although the proportion of Ni^0 at the surface increased with Ni content, for example 56, 67 and 52% of Ni^0 for 5% (0.46:0.54 mol), 10% (0.65:0.35 mol) and 15% (0.39:0.61 mol) Ni-Cu catalysts, respectively. Regarding the BE, the metallic Ni peaks for bimetallic Ni-Cu catalysts shifted to higher energy with the increase in Ni content on the surface, whereas Cu peaks shifted to lower BEs, resulting from the alloy effect on the surface [50]. According to Wu *et al.*, the standard redox potential of Ni^0/ Ni^{2+} (−0.24 V) is much lower than that of Cu^0/Cu^{2+} (+0.34 V), explaining the BE shift observed for the Ni-Cu catalysts as a charge transfer from Ni to Cu (Ni→Cu) [59]. Thus, the alloying resulted in BE changes and depended on the Ni and Cu content. For 10%Ni10%Cu/C, which presented the highest Ni content, the highest BEs were observed for both Cu and Ni peaks, meaning that the larger Ni amount resulted in a higher Ni→Cu charge transfer. This could also explain the differences in activity and selectivity observed for the catalysts, because even if a Ni-rich surface was observed for all bimetallic catalysts after activation, the surface composition barely changed with the increase in Ni content (64.66 and 62% of Ni for 5%, 10% and 15% Ni-Cu catalysts, respectively), as presented in **Table 3**. The better performance of 10%Ni10%Cu/C was related to the increase in the covalency of Ni, keeping Cu close to the metallic state.

Table 3: Binding energy of Cu $2p_{3/2}$ and Ni $2p_{3/2}$ and CuLMM Auger kinetic energy.

	Cu $2p_{3/2}$ (eV)	Cu $2p_{1/2}$ (eV)	CuLMM Auger KE (eV)	Ni $2p_{3/2}$ (eV)	Ni $2p_{1/2}$ (eV)	Ni at surface (%)	$Ni^0/(Ni^0$ +Ni-species) (%)
10%Cu/C	932.8	952.6	918.5	-	-	-	-
5%Ni5%Cu/C	932.6	952.4	918.4	852.7; 853.3	870.0	64	56
10%Ni10%Cu/C	932.7	952.5	918.5	852.8; 854.0	870.2	66	67
15%Ni15%Cu/C	932.5	952.3	918.5	852.6; 853.4	869.9	62	52

Besides lowering the BEs, alloying Ni with Cu also decreases the reduction temperature of nickel [67], hence H_2-TPR analysis of the mono- and bimetallic Ni-Cu catalysts is displayed in Figure 4. For the monometallic Cu-based catalyst, low hydrogen consumption was observed and only one small peak at 317 °C assigned to the reduction of Cu^{2+} to Cu^0 was detected [50, 68]. This confirms the XRD and XPS data, which indicated reduced Cu-species in the bulk and oxidized Cu-species on the surface. For 10% Ni/C catalyst, several peaks were detected corresponding to the reduction of Ni-species. The peaks up to 320 °C were associated to the reduction of interfacial and highly dispersed nanoparticles in which Ni-hydrazine species are reduced to Ni^0 and the peak shoulder at 353 °C was ascribed to the reduction of bulk Ni-hydrazine [50, 69]. In the case of bimetallic catalysts, the reduction of Cu^{2+} and Ni^{2+}-species shifted towards lower temperatures as compared to the monometallic catalysts, indicating that Ni and Cu together have a combined influence on the reducibility of the catalyst. The exception was 5%Ni5%Cu/C, in which the reduction temperature was even higher than that observed for the monometallic 10%Ni/C. This might be related to the fact that this catalyst had the largest particles as indicated by its specific surface area. Three main reduction peaks were observed for 10%Ni10%Cu/C. This was the catalyst with the lowest reduction temperatures. The first reduction peak appears as a shoulder at 238 °C and 274 °C for 10% and 15%Ni-Cu catalysts, respectively, attributed to the reduction of the well-dispersed nanoparticles ($Cu^{2+} \rightarrow Cu^0$). Those lower peaks were not detected for the 5%Ni5%Cu/C catalyst. The other two main peaks centered at 318 and 362

°C, 300 and shoulder at 330 °C, 312 °C, and 356 °C for the 5%, 10%, and 15% Ni-Cu catalysts, respectively, were associated with the reduction of bulk Cu^{2+} and Ni^{2+} species in the alloy to metallic species in the bimetallic Ni-Cu phases [69-71]. Due to the lower content of Ni in 5% and 15% Ni-Cu catalysts, the third peak is less intense, whereas for 10%Ni10%Cu/C, with higher Ni-content, the peaks at 300 and 330 °C overlap. An additional broad peak was observed for this catalyst at 489 °C that was attributed to the methanation of the support, common for Ni nanoparticles on carbon-based supports and described for CNT [69, 72]. The authors reported the lower activity of Ni nanoparticles to catalyze the methanation when Ni–Cu alloys are formed, thus justifying the absence of this peak for the 5%Ni5%Cu and 15%Ni15%Cu catalysts, in which the alloy formation was already discussed. Therefore, the addition of Cu facilitates the reduction of Ni in the bimetallic catalyst although a high Ni-content is necessary to obtain low reduction temperatures. The formation of different Cu- and Ni-rich phases in 10%Ni10%Cu resulted in a more reducible catalyst.

3.2. Optimization of the operating conditions

Considering that the 10%Ni10%Cu/C catalyst was by far the most promising, further studies were performed in order to optimize the catalytic performances. In Figure 5, the effects of catalyst amount, reaction temperature, reaction time, and reaction atmosphere were evaluated. By increasing the catalyst amount, complete conversions were obtained, and the selectivity was slightly improved, reaching a maximum of 95% (Figure 5a). A higher catalyst load in the reactor provides a more efficient mass transfer by providing a greater number of active sites. According to Maki-Arvela *et al.* [73], this effect is marked by an increase in initial reaction rates and an improvement in selectivity. This is explained by the higher substrate conversion rate that can limit the formation of by-products. Nevertheless, mass transfer was not affected any more with catalyst loadings higher than 52 mg, since the selectivity stabilized around

95%. Accordingly, the ideal catalyst amount was 52 mg, where full PA conversion, 94% selectivity to *n*-PD and a high carbon balance (94%) was obtained.

The reaction temperature was evaluated at different temperatures: 250, 300, and 320 °C (Figure 5b). The reaction temperature proved to be an important factor for the catalytic performance, considering that the increase from 250 to 300 °C boosted the conversion from 84% to 100% and up to 84% *n*-PD was obtained. A slight increase of 20 °C to 320 °C improved the selectivity by about 10 %. The temperature of 320 °C used in the previous tests proved to be optimal for the reaction. The carbon balance increased with increasing reaction temperature. At 250 °C it was only 68%, increased to 84% at 300 °C, then further improved to 95% at 320 °C. Analyzing the reaction side-products produced at 250 °C, the formation of unidentified heavy compounds besides traces of *n*-hexadecanol and 1-hexadecenol were detected by GC-MS. The presence of these oxygenated compounds, which are intermediates in the HDO reaction, are indicative of competitive DCX and HDO pathways at this temperature. However, when the reaction was performed at 320 °C, the distribution of the products changed forming the DCX product in high yield (*n*-PD 95%). The HDO side-product was detected in traces (*n*-hexadecane, < 2 % selectivity), showing that the reaction pathway is dependent on temperature and DCX favored at higher temperatures. This corroborates with the studies of Murzin *et al*. [10] that affirms that the DCX reaction is limited by thermodynamics factors, at 300 °C ΔH_{DCX} = 179.1 kJ/mol (endothermic) *vs* ΔH_{HDO} = -115.0 kJ/mol (exothermic). Therefore, it explains why higher *n*-PD yields were obtained at higher temperatures, DCX is more efficient.

The effect of reaction time on activity was also evaluated using the 10%Ni10%Cu/C catalyst for 12 h, as shown in Figure 5c. Within the first 1.5 h, the conversion was complete; however, the selectivity increased with time and reached 95% after 6 h. Longer reaction times apparently favored the product degradation, the *n*-PD yield dropped from 95 to 92% after 12

h. Apparently, in the initial period of reaction time the substrate is completely converted into an intermediate of relatively high molecular mass, difficult to be detected by GC-MS. The consecutive conversion of this intermediate into *n*-PD explains that the observed selectivity increases over time. However, longer reaction times may favor side-reactions such as isomerization and oligomerization [22], pointed out by the slight decrease in selectivity. Indeed, the highest selectivity to *n*-PD was obtained for the test carried out for 6 h.

Having optimized the reaction time (6 h), the temperature (320 °C) and the amount (52 mg) of the 10%Ni10%Cu/C catalyst, the role of hydrogen in the reaction medium was evaluated. Therefore, the reaction was carried out in the absence (pure N_2) and in the presence of hydrogen (10 vol% of H_2 in N_2 (10% H_2)), keeping the pressure at 20 bar (operating pressure at 40 bar), as shown in Fig. 5d. Different product distributions were observed despite complete PA conversion and a carbon balance of 95% was obtained in both cases., The *n*-PD selectivity was lower under nitrogen than at low hydrogen concentration (10% H_2 (59% *vs* 95%), meaning that the change in atmosphere led to different reaction pathways. The side-products formed under inert atmosphere were analyzed and considerable amounts of *n*-pentadecene detected (29% selectivity) besides traces (< 4%) of shorter hydrocarbons such as tetradecane and tridecane (**Table 4**). Using 10% H_2, less than 2% *n*-hexadecane was formed, as previously mentioned.

Table 4. Effect of reaction atmosphere on the catalytic performances of 10%Ni10%Cu/C for the DCX of PA to n-PD. Reaction conditions: T = 320˚C, operating pressure = 40 bar, t = 6 h, stirrer speed = 600 rpm; catalyst loading=52 mg; PA loading = 0.197 mmol.

Atmosphere	X_{PA} [a] (%)	$S_{n\text{-}C15}$ [b] (%)	$S_{1\text{-}C15}$ [b] (%)	S_{C15} [b] (%)	S_{C14} [b] (%)	S_{C16} [b] (%)	Carbon balance
$10\%H_2/N_2$	100	95	-	95	-	<2	97
N_2	100	59	29	88	<4	-	93

[a] X_{PA}: PA conversion; [b] $S_{n\text{-}C15}$: selectivity to *n*-pentadecane, $S_{1\text{-}C15}$: selectivity to 1-pentadecene, S_{C15}: total selectivity to C_{15}, S_{C14}: total selectivity to C_{14}: tetradecane + isotetradecane, S_{C16}: total selectivity to C_{16}: *n*-hexadecane.

In the hydroconversion of FA, three different pathways have been reported: DCX, DCN, and HDO. DCX and HDO reactions are exothermic, while DCN exhibits a relatively modest endothermic effect [16]. Thus, DCX and HDO might be the main pathways for the DCX of FA using Ni-Cu catalysts. The product distribution at 320 °C was 95% *n*-PD (DCX) and less than 2% of *n*-hexadecane and revealed the reactivity order of DCX >> HDO. The presence of several oxygenated compounds at 250 °C (*n*-hexadecanol, 1-hexadecenol, *n*-hexadecanal, cetyl palmitate etc.), and only 10% *n*-PD indicated the order of DCX < HDO and possible other side-reactions. On that basis, a reaction mechanism was proposed (Scheme 1) that PA deoxygenation under hydrogen (10 vol% H_2) occurs via three main routes (DCX (1), DCN (2), HDO (3)), and indirect DCX (4–6). DCX (1) is the main route, wherein PA is directly converted to *n*-PD and CO_2. In DCN (2), *n*-PD is indirectly produced through a DCN followed by dehydration resulting in 1-pentadecene that is further hydrogenated. In the HDO pathway, a hydrogenolysis step produces *n*-hexadecanal and 1-hexadecenol due to a keto-enol tautomerism. Further hydrogenation forms *n*-hexadecanol and a subsequent hydrogenolysis finally produces *n*-hexadecane. At higher temperatures, this pathway is not favored, as confirmed by the catalytic DCX of another substrate, SA. DCX of SA was carried out at the optimized conditions using the 10%Ni10%Cu/C catalyst. The catalytic performance was similar to that obtained with PA (100% conversion, 90% *n*-heptadecane (*n*-HD) selectivity and 90% carbon balance). When analyzing the reaction products by GC-MS, *n*-HD was the main product and octadecane was the only byproduct (<5% selectivity). The product distribution in this case also demonstrated the reactivity order of DCX >> HDO, indicating that the same reaction pathway is followed using both FAs. Other reaction pathways are possible, as shown by DCX (4–5) and esterification (6). The intermediate *n*-hexadecanal formed in the hydrogenolysis step (3) can be dehydrogenated leading to a ketene intermediate,

followed by a DCN and a hydrogenation step to form *n*-PD (4). Otherwise, it can be directly transformed into the desired *n*-PD via DCN (5). The viability of step 4 or 5 is dependent on the type of catalytic sites on the catalyst. The dehydrogenation step often requires acidic sites, while the DCN step involves the adsorption of the carbonyl groups in a favorable position to allow the cleavage of CO [57]. However, it is important to note that step 4 will occur depending on the stability of the ketene intermediate. The other possible side-reaction is the esterification of PA with *n*-hexadecanol resulting in cetyl palmitate (6). This product can be transformed into *n*-hexadecanal and *n*-hexadecanol. Therefore, the latter products are converted as previously mentioned into *n*-PD or *n*-hexadecane, respectively.

The absence of hydrogen during the tests performed under nitrogen led to a very different product distribution, in which, besides *n*-PD (only 59%), side-products related to dehydration (29%) and traces related to cracking and/or isomerization reactions were detected. As the hydrogenolysis reaction is not possible in the absence of hydrogen, only DCX (1) and DCN (2) steps are possible simultaneously forming *n*-pentadecane and 1-pentadecene as the major products In the latter case, 1-pentadecene is formed but the absence of hydrogen prevented its hydrogenation to form the saturated compounds. The disadvantage of having remaining olefins in contact with the catalyst is that secondary reactions such as isomerization and cracking can occur. Therefore, the presence of isomers and shorter hydrocarbons, even in small amounts (< 4%), confirmed that under inert atmosphere pathway 2 is followed, while in the presence of hydrogen pathways 1 or 2 are possible. Because 1-pentadecene is rapidly hydrogenated in the pathway 2, its formation is not detected. This highlights the ability of the catalyst to provide deoxygenation reactions, with DCX being the most relevant at the studied reaction conditions. Hydrogen played an important role regarding the *n*-PD selectivity, because the hydrogenation of the olefins formed by the DCN pathway generated up to 95% *n*-PD. This explained why the low hydrogen concentration (10 vol% H_2) was sufficient to

provide high selectivity. Therefore, the DCX of FA using 10%Ni10%Cu/C was more efficient at 10 vol% H_2 than under inert atmosphere.

In addition to the distinct performance in the catalytic DCX of PA, the 10%Ni10%Cu/C catalyst was recycled 3 times maintaining its conversion without losing activity or selectivity (Figure 6a). The catalyst was characterized after the recyclability test and compared to the activated fresh version in order to verify the catalyst stability at reaction conditions. The TEM analysis of the recycled catalyst is shown in Figure 6b indicating the same particle size and particle size distribution, which might be related to the presence of Ni in the alloy. As reported, the addition of Ni in Cu surfaces is highly beneficial, providing remarkable stability of the nanoparticles against sintering, even at high temperatures (700 °C) [50, 59, 74]. The XRD spectrum of the recycled 10%Ni10%Cu/C catalyst presented the same diffraction peaks and diffraction angles as the fresh catalyst (Figure 6c). In addition, the size of the metal crystallites for the fresh and the recycled catalysts remained unchanged regardless of the diffraction planes considered for the calculation. Based on the Ni (111) plane the crystal size was 12.9 and 12.5 nm for fresh and recycled catalysts, respectively, and that based on the Cu (111) plane was 21.2 and 21.4 nm. However, very small peaks at 41.67° and 46.54° were observed for the recycled catalyst and attributed to respective metal-oxide species. This is probably the result of a superficial oxidation of the catalyst during handling considering that the catalytic tests did not indicate any deactivation. Therefore, these results confirmed that the combination of Ni and Cu increased the stability of the Ni–Cu-based catalyst at reaction conditions.

4. Conclusions

In view of the great potential presented by bio-based derivatives to produce *n*-paraffins, the optimization of catalysts has become essential. We present valuable findings in the development of non-noble metal catalysts for the DCX of FA. A series of non-noble monometallic (Ni, Cu, Fe and Ag) and bimetallic Ni–based catalysts supported on activated carbon was designed for the DCX of PA to *n*-PD. None of the monometallic catalysts yielded more than 11% *n*-PD, although the Ni-catalyst had the highest activity. Thus, Ni was alloyed with these non-noble metals forming Ni-based bimetallic catalysts (Ni-Fe, Ni-Ag, Ni-Cu). The Ni-Cu combination was the most promising significantly improving the catalytic performance. The composition 10%Ni10%Cu/C was the most active achieving high conversion, *n*-PD selectivity and carbon balance (76, 86 and 87%, respectively). The high Ni content of this catalyst resulted in a greater Ni-rich phase after activation. In addition, a higher proportion of Ni^0 on the surface was observed resulting in a higher Ni→Cu charge transfer. Therefore, the high performance was related to the increase of the covalent state of Ni, keeping Cu close to the metallic state. As a consequence, this catalyst displayed the lowest reduction temperatures among the mono- and bimetallic Ni-Cu catalysts. Although the Cu addition facilitated the Ni reduction in the bimetallic catalyst, a high Ni-content was necessary to provide a more reducible catalyst. At optimized reaction conditions (52 mg of activated catalyst, 0.96 g PA·g^{-1}cat, 320 °C, a pressure of 40 bar with 10 vol.% of H_2 in N_2 for 6 h), a yield of 95% *n*-PD was obtained with minimal by-product formation. The high catalytic activity was maintained for 3 cycles without the need for catalyst reactivation. The observed high *n*-PD selectivity of 10%Ni10%Cu/C is due to the fact that DCX is much more favored than HDO among the main reaction pathways. The studies revealed that the main role is played by hydrogen that must be present to guarantee a high *n*-PD production, otherwise considerable quantities of the dehydrogenated intermediate 1-pentadecene remain unconverted. The latter compound in contact with the catalyst might then favor secondary

reactions such as isomerization and cracking. Furthermore, the excellent performances obtained when using SA as substrate for DCX emphasizes the possibility to extend the range of applications for the non-noble Ni-Cu catalysts, to convert other FAs or mixtures of FAs. This is a very promising catalyst for the production of *n*-paraffins from fatty acids derived from vegetable oils. The next steps involve testing the DCX of other FAs and then using the triglycerides directly to obtain *n*-paraffins.

Author Contributions

The manuscript was written through contributions of all authors. All authors have given approval to the final version of the manuscript.

Acknowledgements

This work was supported by Weychem Lamotte Company and Centrale Lille. The authors acknowledge Maya Marinova for the TEM analysis and Martine Trentesaux for the XPS analysis. The REALCAT platform is benefiting from a state subsidy administrated by the French National Research Agency (ANR) within the frame of the 'Investments for the Future' program (PIA), with the contractual reference 'ANR-11-EQPX-0037'. The European Union, through the FEDER funding administered by the Hauts-de-France Region, has co-financed the platform. Centrale Lille, CNRS, and the University of Lille as well as the Centrale Initiatives Foundation, are thanked for their financial contributions to the acquisition and implementation of the equipment of the REALCAT platform. Chevreul Institute (FR 2638), Ministère de l'Enseignement Supérieur et de la Recherche, Hauts-de-France Region and FEDER are also acknowledged. We would like to thank Editage (www.editage.com) for English language editing.

References

[1] F. Dumeignil, M. Capron, B. Katryniok, R. Wojcieszak, A. Löfberg, J.-S. Girardon, S. Desset, M. Araque-Marin, L. Jalowiecki-Duhamel, S. Paul, Biomass-derived Platform Molecules Upgrading through Catalytic Processes: Yielding Chemicals and Fuels, J. Japan Pet. Inst. 58 (2015) 257–273. doi:10.1627/jpi.58.257.

[2] World Energy Primary Production, Energy Production, Enerdata,https://yearbook.enerdata.net/total-energy/, (accessed January 24, 2020).

[3] Fossil-Fuels Depletion, http://www.roperld.com/science/minerals/FossilFuelsDepletion.htm (accessed January 24, 2020).

[4] S. Chu, A. Majumdar, Opportunities and challenges for a sustainable energy future, Nature. 488 (2012) 294–303. doi:10.1038/nature11475.

[5] M.Z. Hossain, M.B.I. Chowdhury, A.K. Jhawar, W.Z. Xu, P.A. Charpentier, Continuous low pressure decarboxylation of fatty acids to fuel-range hydrocarbons with in situ hydrogen production, Fuel. 212 (2018) 470–478. doi:10.1016/j.fuel.2017.09.092.

[6] Z. Hossain, M.B.I. Chowdhury, A.K. Jhawar, W.Z. Xu, M.C. Biesinger, P.A. Charpentier, Continuous Hydrothermal Decarboxylation of Fatty Acids and Their Derivatives into Liquid Hydrocarbons Using Mo/Al2O3 Catalyst, ACS Omega. 3 (2018) 7046–7060. doi:10.1021/acsomega.8b00562.

[7] K. Waldron, Advances in biorefineries : biomass and waste supply chain exploitation, Woodhead Publishing, 2014.

[8] A.K. Kumar, S. Sharma, Recent updates on different methods of pretreatment of lignocellulosic feedstocks: a review, Bioresour. Bioprocess. 4 (2017). doi:10.1186/s40643-017-0137-9.

[9] A. Sivasamy, K.Y. Cheah, P. Fornasiero, F. Kemausuor, S. Zinoviev, S. Miertus, Catalytic applications in the production of biodiesel from vegetable oils, ChemSusChem. 2 (2009) 278–300. doi:10.1002/cssc.200800253.

[10] M. Snåre, I. Kubičková, P. Mäki-Arvela, K. Eränen, D.Y. Murzin, Heterogeneous Catalytic Deoxygenation of Stearic Acid for Production of Biodiesel, Ind. Eng. Chem. Res. 45 (2006) 5708–5715. doi:10.1021/ie060334i.

[11] M.Z. Hossain, A.K. Jhawar, M.B.I. Chowdhury, W.Z. Xu, W. Wu, D. V. Hiscott, P.A. Charpentier, Using Subcritical Water for Decarboxylation of Oleic Acid into Fuel-Range Hydrocarbons, Energy & Fuels. 31 (2017) 4013–4023. doi:10.1021/acs.energyfuels.6b03418.

[12] J. Fu, X. Lu, P.E. Savage, Hydrothermal Decarboxylation and Hydrogenation of Fatty Acids over Pt/C, ChemSusChem. 4 (2011) 481–486. doi:10.1002/cssc.201000370.

[13] J. Fu, F. Shi, L.T. Thompson, X. Lu, P.E. Savage, Activated Carbons for Hydrothermal Decarboxylation of Fatty Acids, ACS Catal. 1 (2011) 227–231. doi:10.1021/cs1001306.

[14] J. Fu, X. Lu, P.E. Savage, Catalytic hydrothermal deoxygenation of palmitic acid, in: Energy Environ. Sci., Royal Society of Chemistry, 2010: pp. 311–317. doi:10.1039/b923198f.

[15] E. Santillan-Jimenez, M. Crocker, Catalytic deoxygenation of fatty acids and their derivatives to hydrocarbon fuels via decarboxylation/decarbonylation, J. Chem. Technol. Biotechnol. 87 (2012) 1041–1050. doi:10.1002/jctb.3775.

[16] Ł. Jęczmionek, K. Porzycka-Semczuk, Hydrodeoxygenation, decarboxylation and decarbonylation reactions while co-processing vegetable oils over a NiMo hydrotreatment catalyst. Part I: Thermal effects - Theoretical considerations, Fuel. 131 (2014) 1–5. doi:10.1016/j.fuel.2014.04.055.

[17] Heavy Liquid Paraffin by Adinath Chemicals, http://www.adinathchemicals.com/liquid-paraffin-oil/heavy-liquid-paraffin.html (accessed January 24, 2020).

[18] Heavy Liquid Paraffin by Gandhar Oil, https://www.gandharoil.com/en/businesses/liquid-paraffins-white-oils-petroleum-jelly/heavy-liquid-paraffin/ (accessed January 24, 2020).

[19] H. W. Stache, Anionic Surfactants: Organic Chemistry - Surfactant science series, CRC Press, 1995.

[20] D. Y. Murzin, I. Kubičková, M. Snåre, P. Mäki-Arvela and J. Myllyoja, 2006. Method for the manufacture of hydrocarbons. Patent WO2006075057.

[21] Paraffin Oil - an overview, ScienceDirect Topics, https://www.sciencedirect.com/topics/engineering/paraffin-oil (accessed January 24, 2020).

[22] B.P. Pattanaik, R.D. Misra, Effect of reaction pathway and operating parameters on the deoxygenation of vegetable oils to produce diesel range hydrocarbon fuels: A review, Renew. Sustain. Energy Rev. 73 (2017) 545–557. doi:10.1016/j.rser.2017.01.018.

[23] G.J.S. Dawes, E.L. Scott, J. Le Nôtre, J.P.M. Sanders, J.H. Bitter, Deoxygenation of biobased molecules by decarboxylation and decarbonylation - A review on the role of heterogeneous, homogeneous and bio-catalysis, Green Chem. 17 (2015) 3231–3250. doi:10.1039/c5gc00023h.

[24] D. Li, H. Xin, X. Du, X. Hao, Q. Liu, C. Hu, Recent advances for the production of hydrocarbon biofuel via deoxygenation progress, Sci. Bull. 60 (2015) 2096–2106. doi:10.1007/s11434-015-0971-0.

[25] B. Veriansyah, J.Y. Han, S.K. Kim, S.A. Hong, Y.J. Kim, J.S. Lim, Y.W. Shu, S.G. Oh, J. Kim, Production of renewable diesel by hydroprocessing of soybean oil: Effect of catalysts, Fuel. 94 (2012) 578–585. doi:10.1016/j.fuel.2011.10.057.

[26] J.G. Immer, M.J. Kelly, H.H. Lamb, Catalytic reaction pathways in liquid-phase deoxygenation of C18 free fatty acids, Appl. Catal. A Gen. 375 (2010) 134–139. doi:10.1016/j.apcata.2009.12.028.

[27] K.A. Rogers, Y. Zheng, Selective Deoxygenation of Biomass-Derived Bio-oils within Hydrogen-Modest Environments: A Review and New Insights, ChemSusChem. 9 (2016) 1750–1772. doi:10.1002/cssc.201600144.

[28] R.W. Gosselink, D.R. Stellwagen, J.H. Bitter, Tungsten-Based Catalysts for Selective Deoxygenation, Angew. Chemie Int. Ed. 52 (2013) 5089–5092. doi:10.1002/anie.201209809.

[29] J. Wu, J. Shi, J. Fu, J.A. Leidl, Z. Hou, X. Lu, Catalytic decarboxylation of fatty acids to aviation fuels over nickel supported on activated carbon, Sci. Rep. 6 (2016). doi:10.1038/srep27820.

[30] C. Yang, R. Nie, J. Fu, Z. Hou, X. Lu, Production of aviation fuel via catalytic hydrothermal decarboxylation of fatty acids in microalgae oil, Bioresour. Technol. 146 (2013) 569–573. doi:10.1016/j.biortech.2013.07.131.

[31] H. Ohta, H. Kobayashi, K. Hara, A. Fukuoka, Hydrodeoxygenation of phenols as lignin models under acid-free conditions with carbon-supported platinum catalysts, Chem. Commun. 47 (2011) 12209–12211. doi:10.1039/c1cc14859a.

[32] L. Faba, E. Díaz, A. Vega, S. Ordóñez, Hydrodeoxygenation of furfural-acetone condensation adducts to tridecane over platinum catalysts, Catal. Today. 269 (2016) 132–139. doi:10.1016/j.cattod.2015.09.055.

[33] C. Liu, J. Sun, H.M. Brown, O.G. Marin-Flores, J.T. Bays, A.M. Karim, Y. Wang, Aqueous phase hydrodeoxygenation of polyols over Pd/WO 3 -ZrO 2 : Role of Pd-WO 3 interaction and hydrodeoxygenation pathway, Catal. Today. 269 (2016) 103–109. doi:10.1016/j.cattod.2015.10.034.

[34] P. Duan, X. Bai, Y. Xu, A. Zhang, F. Wang, L. Zhang, J. Miao, Catalytic upgrading of crude algal oil using platinum/gamma alumina in supercritical water, Fuel. 109 (2013) 225–233. doi:10.1016/j.fuel.2012.12.074.

[35] P. Duan, P.E. Savage, Upgrading of crude algal bio-oil in supercritical water, Bioresour. Technol. 102 (2011) 1899–1906. doi:10.1016/j.biortech.2010.08.013.

[36] E. Santillan-Jimenez, T. Morgan, J. Lacny, S. Mohapatra, M. Crocker, Catalytic deoxygenation of triglycerides and fatty acids to hydrocarbons over carbon-supported nickel, in: Fuel, 2013: pp. 1010–1017. doi:10.1016/j.fuel.2012.08.035.

[37] I. Kubičková, M. Snåre, K. Eränen, P. Mäki-Arvela, D.Y. Murzin, Hydrocarbons for diesel fuel via decarboxylation of vegetable oils, Catal. Today. 106 (2005) 197–200. doi:10.1016/J.CATTOD.2005.07.188.

[38] R.W. Gosselink, S.A.W. Hollak, S.-W. Chang, J. van Haveren, K.P. de Jong, J.H. Bitter, D.S. van Es, Reaction Pathways for the Deoxygenation of Vegetable Oils and Related Model Compounds, ChemSusChem. 6 (2013) 1576–1594. doi:10.1002/cssc.201300370.

[39] P. Mäki-Arvela, M. Snåre, K. Eränen, J. Myllyoja, D.Y. Murzin, Continuous decarboxylation of lauric acid over Pd/C catalyst, Fuel. 87 (2008) 3543–3549. doi:10.1016/j.fuel.2008.07.004.

[40] I. Simakova, O. Simakova, P. Mäki-Arvela, A. Simakov, M. Estrada, D.Y. Murzin, Deoxygenation of palmitic and stearic acid over supported Pd catalysts: Effect of metal dispersion, Appl. Catal. A Gen. 355 (2009) 100–108. doi:10.1016/j.apcata.2008.12.001.

[41] J.G. Immer, H.H. Lamb, Fed-Batch Catalytic Deoxygenation of Free Fatty Acids, Energy & Fuels. 24 (2010) 5291–5299. doi:10.1021/ef100576z.

[42] E.W. Ping, J. Pierson, R. Wallace, J.T. Miller, T.F. Fuller, C.W. Jones, On the nature of the deactivation of supported palladium nanoparticle catalysts in the

decarboxylation of fatty acids, Appl. Catal. A Gen. 396 (2011) 85–90. doi:10.1016/j.apcata.2011.01.042.

[43] A.S. Berenblyum, R.S. Shamsiev, T.A. Podoplelova, V.Y. Danyushevsky, The influence of metal and carrier natures on the effectiveness of catalysts of the deoxygenation of fatty acids into hydrocarbons, Russ. J. Phys. Chem. A. 86 (2012) 1199–1203. doi:10.1134/S0036024412070023.

[44] A. Kiméné, R. Wojcieszak, S. Paul, F. Dumeignil, Catalytic decarboxylation of fatty acids to hydrocarbons over non-noble metal catalysts: the state of the art, J. Chem. Technol. Biotechnol. 94 (2019) 658–669. doi:10.1002/jctb.5776.

[45] P. R. Green, J. J. Scheibel, D. I. Collias, 2012 . Bio-based linear alkylphenyl sulfonates. Patent WO2012112828.

[46] S. De, J. Zhang, R. Luque, N. Yan, Ni-based bimetallic heterogeneous catalysts for energy and environmental applications, Energy Environ. Sci. 9 (2016) 3314–3347. doi:10.1039/c6ee02002j.

[47] M. Zielinski, R. Wojcieszak, S. Monteverdi, M. Mercy, M.M. Bettahar, Catal. Comm. 6 (2005) 777-783

[48] Replacing Critical Materials with Abundant Materials - The Role of the Chemical Sciences in Finding Alternatives to Critical Resources - NCBI Bookshelf, https://www.ncbi.nlm.nih.gov/books/NBK100035/ (accessed January 24, 2020).

[49] Palladium Silver Ratio Charts - 5 Years, BullionByPost, https://www.bullionbypost.co.uk/price-ratio/palladium-silver-ratio-chart/ (accessed February 10, 2020).

[50] A.B. Dongil, B. Bachiller-Baeza, I. Rodríguez-Ramos, J.L.G. Fierro, N. Escalona, The effect of Cu loading on Ni/carbon nanotubes catalysts for hydrodeoxygenation of guaiacol, RSC Adv. 6 (2016) 26658–26667. doi:10.1039/c6ra00041j.

[51] X. Yu, J. Chen, T. Ren, Promotional effect of Fe on performance of Ni/SiO2 for deoxygenation of methyl laurate as a model compound to hydrocarbons, RSC Adv. 4 (2014) 46427–46436. doi:10.1039/c4ra07932a.

[52] D.M. Alonso, S.G. Wettstein, J.A. Dumesic, Bimetallic catalysts for upgrading of biomass to fuels and chemicals, Chem. Soc. Rev. 41 (2012) 8075–8098. doi:10.1039/c2cs35188a.

[53] C. Denk, S. Foraita, L. Kovarik, K. Stoerzinger, Y. Liu, E. Baráth, J.A. Lercher, Rate enhancement by Cu in NixCu1-x/ZrO2 bimetallic catalysts for hydrodeoxygenation of stearic acid, Catal. Sci. Technol. 9 (2019) 2620–2629. doi:10.1039/c9cy00181f.

[54] R. Loe, E. Santillan-Jimenez, T. Morgan, L. Sewell, Y. Ji, S. Jones, M.A. Isaacs, A.F. Lee, M. Crocker, Effect of Cu and Sn promotion on the catalytic deoxygenation of model and algal lipids to fuel-like hydrocarbons over supported Ni catalysts, Appl. Catal. B Environ. 191 (2016) 147–156. doi:10.1016/j.apcatb.2016.03.025.

[55] A.K. Singh, Q. Xu, Synergistic Catalysis over Bimetallic Alloy Nanoparticles, ChemCatChem. 5 (2013) 652–676. doi:10.1002/cctc.201200591.

[56] N. Toshima, T. Yonezawa, Bimetallic nanoparticles - Novel materials for chemical and physical applications, New J. Chem. 22 (1998) 1179–1201. doi:10.1039/a805753b.

[57] H.H. Kung, M.C. Kung, Nanotechnology and Heterogeneous Catalysis, in: Nanotechnol. Catal., Springer New York, New York, NY, 2008: pp. 1–11. doi:10.1007/978-0-387-34688-5_1.

[58] I. Zegkinoglou, L. Pielsticker, Z.K. Han, N.J. Divins, D. Kordus, Y.T. Chen, C. Escudero, V. Pérez-Dieste, B. Zhu, Y. Gao, B.R. Cuenya, Surface Segregation in CuNi Nanoparticle Catalysts during CO 2 Hydrogenation: The Role of CO in the Reactant Mixture, J. Phys. Chem. C. 123 (2019) 8421–8428. doi:10.1021/acs.jpcc.8b09912.

[59] D. Wu, W. Zhang, D. Cheng, Facile Synthesis of Cu/NiCu Electrocatalysts Integrating Alloy, Core–Shell, and One-Dimensional Structures for Efficient Methanol Oxidation Reaction, ACS Appl. Mater. Interfaces. 9 (2017) 19843–19851. doi:10.1021/acsami.7b03876.

[60] A.R. Denton, N.W. Ashcroft, Vegards law, Phys. Rev. A. 43 (1991) 3161–3164. doi:10.1103/PhysRevA.43.3161.

[61] J. Feng, C.-P. Zhang, Preparation of Cu–Ni alloy nanocrystallites in water-in-oil microemulsions, J. Colloid Interface Sci. 293 (2006) 414–420. doi:10.1016/j.jcis.2005.06.071.

[62] F. Bonet, S. Grugeon, L. Dupont, R. Herrera Urbina, C. Guéry, J.M. Tarascon, Synthesis and characterization of bimetallic Ni-Cu particles, J. Solid State Chem. 172 (2003) 111–115. doi:10.1016/S0022-4596(02)00163-9.

[63] S. Radiman, G.H. Mohamed Saeed, S.S. Gasaymeh, H.N. Lim, N.M. Huang, Mild hydrothermal synthesis of NiCu nanoparticles, J. Nanomater. 2010 (2010). doi:10.1155/2010/184137.

[64] K.K. Patra, P.A. Bharad, V. Jain, C.S. Gopinath, Direct solar-to-hydrogen generation by quasi-artificial leaf approach: possibly scalable and economical device, J. Mater. Chem. A. 7 (2019) 3179–3189. doi:10.1039/C8TA11307F.

[65] V.M. Shinde, G. Madras, Nanostructured Pd modified Ni/CeO2 catalyst for water gas shift and catalytic hydrogen combustion reaction, Appl. Catal. B Environ. 132–133 (2013) 28–38. doi:10.1016/j.apcatb.2012.11.021.

[66] I. Czekaj, F. Loviat, F. Raimondi, J. Wambach, S. Biollaz, A. Wokaun, Characterization of surface processes at the Ni-based catalyst during the methanation of biomass-derived synthesis gas: X-ray photoelectron spectroscopy (XPS), Appl. Catal. A Gen. 329 (2007) 68–78. doi:10.1016/j.apcata.2007.06.027.

[67] A.R. Naghash, T.H. Etsell, S. Xu, XRD and XPS study of Cu-Ni interactions on reduced copper-nickel-aluminum oxide solid solution catalysts, Chem. Mater. 18 (2006) 2480–2488. doi:10.1021/cm051910o.

[68] A. Jha, D.W. Jeong, W.J. Jang, C. V. Rode, H.S. Roh, Mesoporous NiCu-CeO2 oxide catalysts for high-temperature water-gas shift reaction, RSC Adv. 5 (2015) 1430–1437. doi:10.1039/c4ra13142h.

[69] Q. Ma, D. Wang, M. Wu, T. Zhao, Y. Yoneyama, N. Tsubaki, Effect of catalytic site position: Nickel nanocatalyst selectively loaded inside or outside carbon nanotubes for methane dry reforming, Fuel. 108 (2013) 430–438. doi:10.1016/j.fuel.2012.12.028.

[70] X. Chen, S.A.C. Carabineiro, S.S.T. Bastos, P.B. Tavares, J.J.M. Órfão, M.F.R. Pereira, J.L. Figueiredo, Exotemplated copper, cobalt, iron, lanthanum and nickel oxides for catalytic oxidation of ethyl acetate, J. Environ. Chem. Eng. 1 (2013) 795–804. doi:10.1016/j.jece.2013.07.019.

[71] M.M. Ambursa, T.H. Ali, H.V. Lee, P. Sudarsanam, S.K. Bhargava, S.B.A. Hamid, Hydrodeoxygenation of dibenzofuran to bicyclic hydrocarbons using bimetallic Cu-Ni catalysts supported on metal oxides, Fuel. 180 (2016) 767–776. doi:10.1016/j.fuel.2016.04.045.

[72] A. Nieto-Márquez, S. Gil, A. Romero, J.L. Valverde, S. Gómez-Quero, M.A. Keane, Gas phase hydrogenation of nitrobenzene over acid treated structured and amorphous carbon supported Ni catalysts, Appl. Catal. A Gen. 363 (2009) 188–198. doi:10.1016/j.apcata.2009.05.016.

[73] P. Mäki-Arvela, I. Kubickova, M. Snåre, K. Eränen, D.Y. Murzin, Catalytic Deoxygenation of Fatty Acids and Their Derivatives, Energy & Fuels. 21 (2007) 30–41. doi:10.1021/ef060455v.

[74] R. Watanabe, T. Ishizaki, Enhancement of pressure-free bonding with Cu particles by the addition of Cu-Ni alloy nanoparticles, J. Mater. Chem. C. 2 (2014) 3542–3548. doi:10.1039/c4tc00240g.

Figure 1. Activity of (a) non-noble monometallic, (b) Ni-based bimetallic, (c) Ni-Cu bimetallic catalysts for DCX of PA into *n*-PD. Reaction conditions: T = 320 °C, 40 bar operating pressure, t = 6 h, stirrer speed = 600 rpm; catalyst amount = 12.8 mg, PA loading = 0.197 mmol. PA conversion (blue), *n*-PD selectivity (orange), *n*-PD yield (gray), and carbon balance (yellow line).

Figure 2. TEM images of 10%Ni10%Cu/C catalyst before (a) and after (b) activation under hydrogen.

Figure 3. XRD patterns of (a) fresh and (b) activated catalysts with different metal loadings; (c) XRD peak of (111) plane in Ni-Cu bimetallic catalysts; (d) XPS spectra in the Cu 2p and (e) Ni 2p region for the bimetallic Ni-Cu catalysts after activation and (f) in the Ni $2p_{3/2}$ region for 10%Ni10%Cu/C catalyst.

Figure 4. TPR profiles of the mono and bimetallic catalysts

Figure 5. DCX of PA into *n*-PD using 10%Ni10%Cu/C catalyst: (a) catalytic activity versus mass of catalyst, (b) reaction temperature, (c) reaction time and (d) reaction atmosphere. Reaction condition: T = 320°C, operating pressure = 40 bar, t = 6 h, stirrer speed = 600 rpm; catalyst amount = 52 mg, PA loading = 0.197 mmol. PA conversion (blue), *n*-PD selectivity (orange), *n*-PD yield (gray), carbon balance (yellow line).

Figure 6. DCX of PA into *n*-PD using 10%Ni10%Cu/C catalyst: a) catalytic activity in recycling tests, b) Particle size distribution from TEM images, and c) XRD patterns of activated and recycled catalyst.

Scheme 1. Proposed mechanism for DO [44].

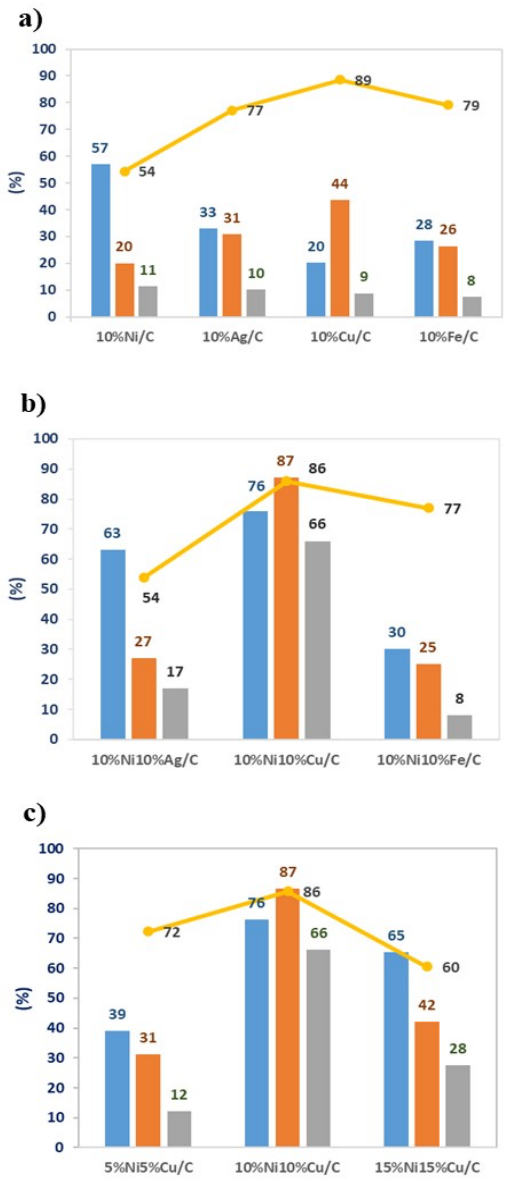

Figure 1. Activity of (a) non-noble monometallic, (b) Ni-based bimetallic, (c) Ni-Cu bimetallic catalysts for DCX of PA into *n*-PD. Reaction conditions: T = 320 °C, 40 bar operating pressure, t = 6 h, stirrer speed = 600 rpm; catalyst amount = 12.8 mg, PA loading = 0.197 mmol. PA conversion (blue), *n*-PD selectivity (orange), *n*-PD yield (gray), and carbon balance (yellow line).

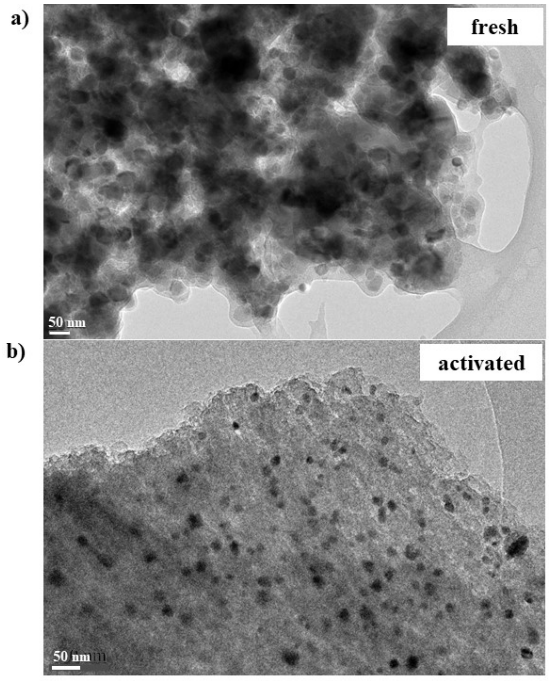

Figure 2. TEM images of 10%Ni10%Cu/C catalyst before (a) and after (b) activation under hydrogen.

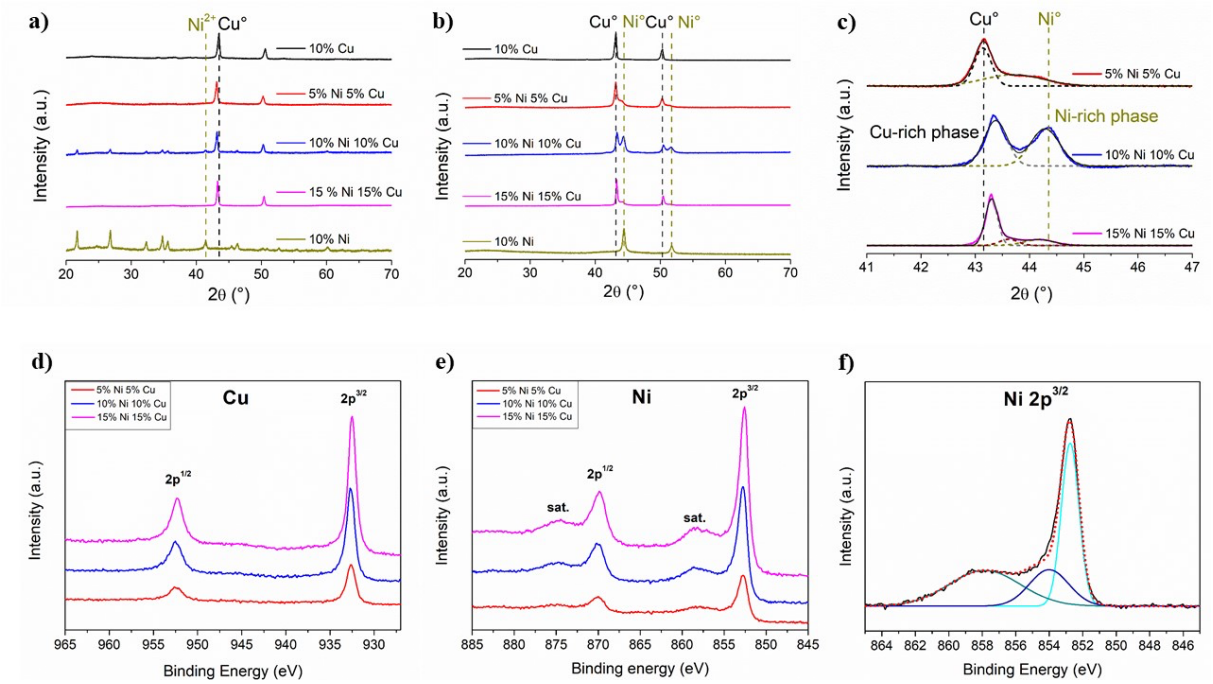

Figure 3. XRD patterns of (a) fresh and (b) activated catalysts with different metal loadings; (c) XRD peak of (111) plane in Ni-Cu bimetallic catalysts; (d) XPS spectra in the Cu 2p and (e) Ni 2p region for the bimetallic Ni-Cu catalysts after activation and (f) in the Ni $2p^{3/2}$ region for 10%Ni10%Cu/C catalyst.

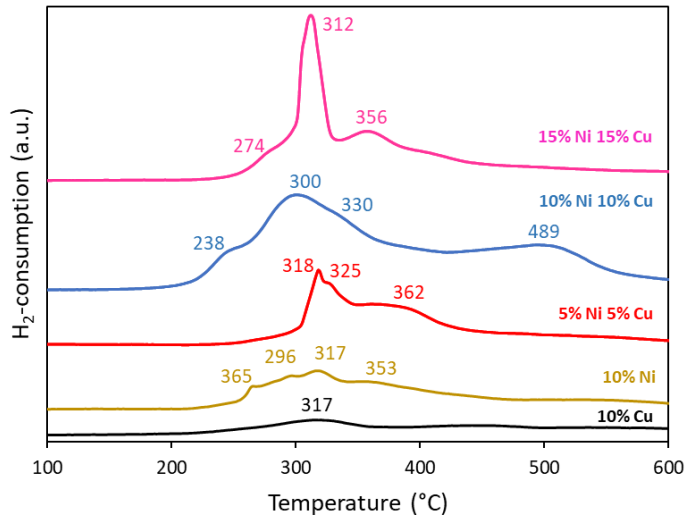

Figure 4. TPR profiles of the mono and bimetallic catalysts

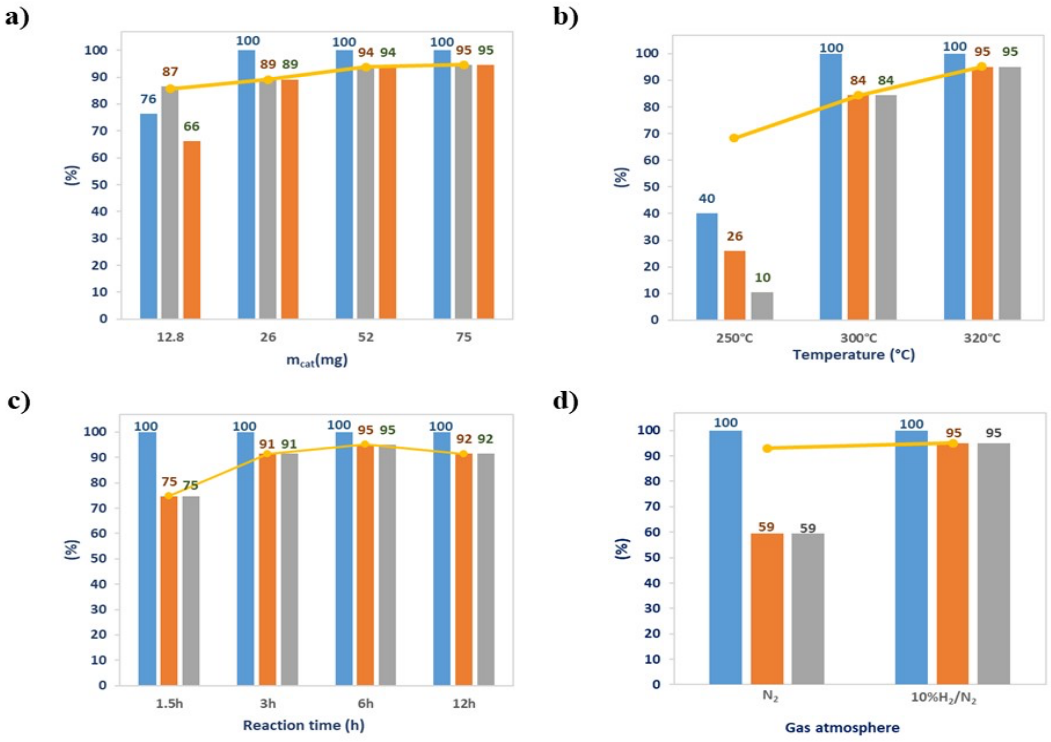

Figure 5. DCX of PA into *n*-PD using 10%Ni10%Cu/C catalyst: (a) catalytic activity versus mass of catalyst, (b) reaction temperature, (c) reaction time and (d) reaction atmosphere. Reaction condition: T = 320°C, operating pressure = 40 bar, t = 6 h, stirrer speed = 600 rpm; catalyst amount = 52 mg, PA loading = 0.197 mmol. PA conversion (blue), *n*-PD selectivity (orange), *n*-PD yield (gray), carbon balance (yellow line).

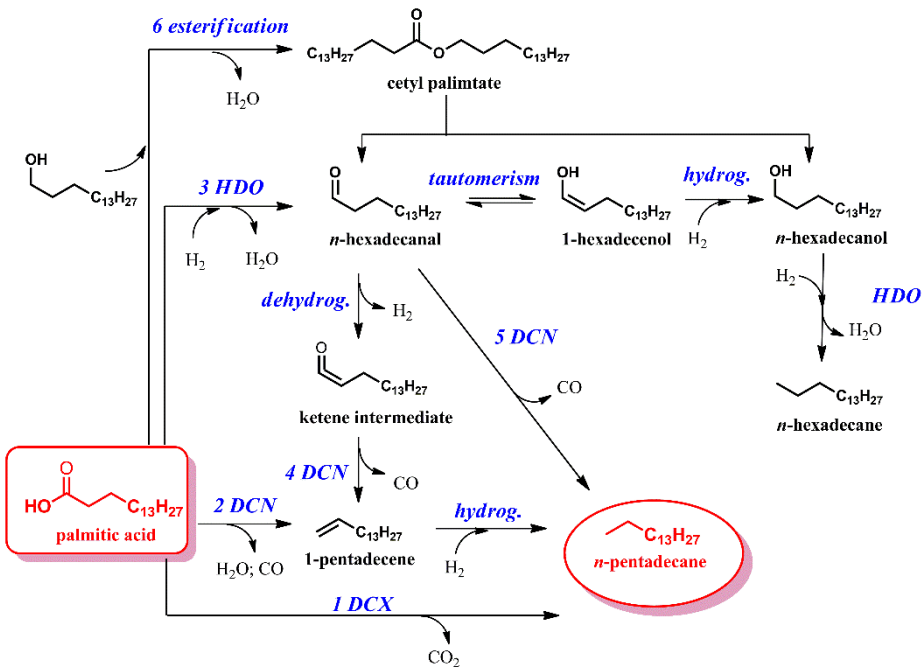

Scheme 1. Proposed mechanism for DO.[44]

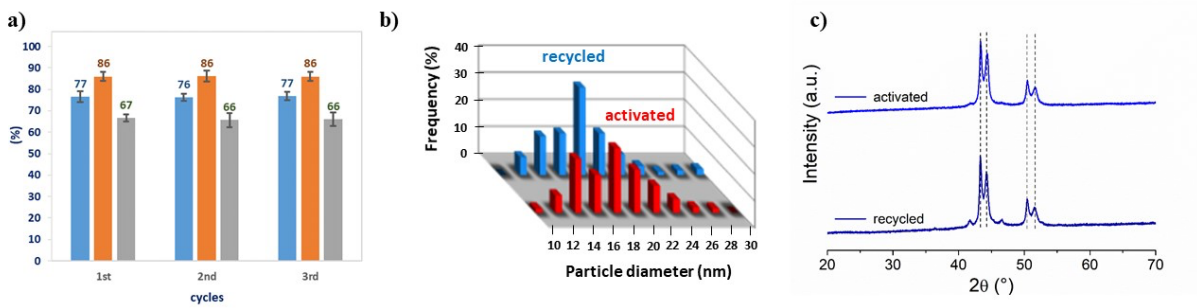

Figure 6. DCX of PA into *n*-PD using 10%Ni10%Cu/C catalyst: a) catalytic activity in recycling tests, b) Particle size distribution from TEM images, and c) XRD patterns of activated and recycled catalyst.